Research Article

Microstructural softening induced adiabatic shear banding in Ti-23Nb-0.7Ta-2Zr-O gum metal

Silu Liu [a], Y.Z. Guo [b], Z.L. Pan [c], X.Z. Liao [d], E.J. Lavernia [e], Y.T. Zhu [f,a], Q.M. Wei [c], Yonghao Zhao [a,*]

[a] Nano and Heterogeneous Materials Center, School of Materials Science and Engineering, Nanjing University of Science and Technology, Nanjing 210094, China
[b] School of Aeronautics, Northwestern Polytechnical University, Xi'an 710072, China
[c] Department of Mechanical Engineering, University of North Carolina at Charlotte, NC 28223-0001, USA
[d] School of Aerospace, Mechanical and Mechatronic Engineering, The University of Sydney, NSW 2006, Australia
[e] Department of Materials Science and Engineering, University of California, Irvine, CA 92697, USA
[f] Department of Materials Science and Engineering, North Carolina State University, NC 27695, USA

ARTICLE INFO

ABSTRACT

Ti-23Nb-0.7Ta-2Zr-O gum metal (GM) is an attractive candidate material for applications that require superior mechanical properties. In our earlier investigation of the GM [1], geometrical softening and the generation of adiabatic shear bands (ASBs) were proposed as primary reasons for the documented anisotropic impact response. In the present study, electron backscattered diffraction (EBSD) analysis reveals two different deformed microstructures, i.e., deformed ultrafine grains (UFGs) and dynamically recrystallized UFGs, formed in the ASBs of GM samples processed by extrusion equal channel angular pressing (ECAP), respectively. Additional calculation of temperature rise during dynamic compression suggests that the above microstructure differences in the ASBs was originated from their different maximum ASB temperatures (608 K for extruded GM and 1159 K for ECAP-processed GM). Moreover, our calculation on the temperature at the onset of ASBs indicates that microstructural softening is the primary cause for the development of ASBs in both extruded GM (321 K) and ECAP-processed GM (331 K).

© 2020 Published by Elsevier Ltd on behalf of The editorial office of Journal of Materials Science & Technology.

1. Introduction

Initially designed on the basis of *ab initio* calculations, gum metals (GMs) include a group of β-Ti alloys with body-centered cubic (bcc) structure and "super" mechanical properties such as super strength, super elasticity with relatively low elastic modulus, super plasticity and so on [1–10]. Despite the obvious advantages of using GMs for applications that require exceptional mechanical performance, only limited and sometimes contradictory information exists on the behavior of GMs under dynamic deformation conditions. In fact, inspection of the published literatures reveal a number of publications debating the origins of the underlying deformation mechanisms [11–19] with particular interest in the origins of the adiabatic shear bands (ASBs) that are widely observed during dynamic loading [20–23].

In our earlier study [1], we proposed that geometrical softening is responsible for the observed anisotropic impact behavior and ASB formation in the GM loaded in the transverse direction (TD). In this study we introduced specific textures into a GM via extrusion and equal channel angular pressing (ECAP), and then dynamically loaded the materials in the TD and extrusion direction (ED) orientations. Schmid factor analysis was then used to quantify the resolved shear stresses on the different orientations of the textures. Our results showed that ASB formation and catastrophic failure are generated only if the loading direction is perpendicular to the ED and if single-direction shearing is activated. This phenomenon is termed as geometrical softening [1]. In the microstructural evolution of ASBs therein [1], grain rotation and refinement are ascribed as the mechanism responsible for the formation of ultrafine grains (UFGs) inside the ASBs.

Since the early work in Ref. [21], a wide body of literatures have firmly established the importance of ASBs during dynamic deformation. When deformed under dynamic compression, materials initially experience uniform deformation due to strain hardening.

Subsequently, the onset of inhomogeneous deformation occurs as the materials are unable to sustain the strain hardening required to maintain homogeneous deformation. In the case of dynamic loading, the associated high strain rates lead to deformation that occurs in an extremely short time scale, such as milliseconds. Once the deformation becomes inhomogeneous and localized shear develops, most of the plastic deformation is immediately converted into adiabatic heat leading to localized temperature increases. As a consequence, ASBs form in a localized manner and are governed by the competition between strain hardening and thermal softening of the material [20–23].

Dating back to 1944, Zener and Hollomon interpreted the onset of ASBs as a thermo-mechanically coupled competition between thermal softening and strain or strain rate hardening [24]. Since this original analysis, temperature induced softening has been defined as the onset of inhomogeneous deformation in many physical and mathematical analyses on ASBs [25]. Furthermore, observations of recrystallization in narrow regions support the suggestion of a localized temperature rise during the evolution of ASBs [26]. As such, thermal softening is widely accepted to be the cause for the formation of ASBs during dynamic deformation. More recently, however, various investigators have challenged the notion that thermal effects play a critical role during the formation of ASBs. For example, Rittel et al. [27] conducted a series of high strain rate experiments, such as interrupted dynamic tests, dynamic tests with adjusted temperatures and so on. This research indicates that the homogeneous specimen temperature (either adiabatic rise or from test conditions) prior to strain localization has a very minor influence on the subsequent ASB formation, emphasizing the importance of cold work independent of thermal heating [27]. In another study [28], it was reported that dynamic recrystallization precedes adiabatic shear failure (thermal effect excluded) and it's likely to be a dominant micro-mechanical factor in the generation of the ASBs. From these findings one could argue that ASBs are not only a mechanical instability, but are also closely related to the evolution of the microstructure during deformation [28]. In a recently published study Guo et al. [25] argued that the well-accepted thermal softening mechanism associated with ASB formation needs to be reconsidered. In contrast to the accepted correlation between temperature rise, ASB formation and the loss of load capacity, Guo et al. reported a stress drop prior to the formation of ASBs followed by an immediate temperature increase [25]. These results are in stark contradiction to the accepted sequence of events leading to the formation of ASBs.

It is important to establish what are the factors that influence the propensity for the occurrence of ASBs. Interestingly, there are differing assumptions as to the critical elements that are necessary to trigger the formation of ASBs [20–23,29–35]. Some authors state that a certain amount of strain is required for the nucleation of ASBs [20]. Others report that a certain level of strain rate is required to initiate ASBs [20]. Recently, the concept of a critical dynamic mechanical energy has been proposed based on information obtained from mechanical behavior experiments [27].

Motivated by our less than perfect understanding of the mechanisms that govern the formation of ASBs, we used electron backscattered diffraction (EBSD) analysis [36–40] to investigate microstructural evolution during split Hopkinson bar (SHPB) testing of extruded and ECAP processed Ti-23Nb-0.7Ta-2Zr-O. The initial GMs, processed by extrusion and extrusion followed by ECAP [41–44], have different microstructures including grain size, texture and stored energy (dislocation density, misorientation and grain boundary, GB). Following dynamic loading, it is important to carefully characterize the microstructure; unfortunately, there is limited information on the use of EBSD to study the formation of ASBs [37–40]. Moreover, in our study we analyze temperature increases associated with microstructural softening inside ASBs on the basis of mechanical data and using an empirical theoretical framework.

2. Experimental procedures

The initial ingot, which was 0.05 m in diameter and 0.17 m in length, was made of high purity Ti, Nb, Ta and Zr powder through vacuum arc melting and casting. The nominal composition is reported in Ref. [23]. Encapsulated during vacuum arc melting, the powder was wrapped by a protective layer of Ti film to avoid contamination. This ensures that the microstructure and composition of the ingot should remain largely homogeneous. A 0.02-meter-diameter billet was obtained via extruding the ingot at 1283 K. Subsequently, severe plastic deformation was imposed on the extruded billet through one pass of ECAP. The ECAP facility employed a stationary constraint die with channel diameter of 0.02 m and channel angle of 120°. ECAP was performed at 773 K with no back pressure. Extrusion direction in ECAP remained the same as in the prior extrusion process. Henceforth for simplicity, extruded GM and ECAP processed GM will be designated as Extruded-GM and ECAP-GM, respectively.

Samples with dimensions of 0.003 m × 0.003 m × 0.003 m for high strain rate uni-axial compression were sectioned from Extruded-GM and ECAP-GM using wire electrode discharge machining (EDM). High strain rate uni-axial loading was performed using a Kolsky bar system (or SHPB system). For details of the working principles as well as the cautions and caveats of the Kolsky bar technique, see Refs. [31,32,43,44]. Loading direction was perpendicular to the extrusion direction along TD. Dynamically loaded Extruded-GM and ECAP-GM are hereby designated as Extruded-GM-DY and ECAP-GM-DY respectively. For more information regarding sample coordinate system and loading direction, please see Fig. 1.

In preparation for EBSD scanning, samples were mechanically ground using a Buehler EcoMet 250/AutoMet 250 system. Afterwards, they were electro-polished by Buehler electromet-4 using an electrolyte of 90 vol.% acetic acid and 10 vol.% perchloric acid at 45 V, room temperature. Zeiss Ultra equipped with Oxford Instruments Aztec 2.0 EBSD system was used to further characterize the microstructures of the electro-polished samples. The ED-TD planes of Extruded-GM and ECAP-GM were scanned to collect microstructure information, while the ND-TD planes of Extruded-GM-DY and ECAP-GM-DY were scanned. The commercial software Channel 5 was used to optimize the EBSD data, including removal of non-indexed and mis-indexed pixels [37], and to further analyze information of grain size, texture, GB and misorientation etc.

3. Results

3.1. Mechanical properties

Fig. 2 shows the engineering strain-stress curves of Extruded-GM and ECAP-GM. In the stage of uniform deformation, the stresses of these two samples increased to maximum values and then remained as stress plateaus. The stress plateaus ended before the abrupt stress drops which were caused by localized deformation [25,53]. The end points of stress plateaus are 1212 MPa/8.6% (Extruded-GM) and 1381 MPa/11.0% (ECAP-GM) respectively, as listed in Table 1. Following the attainment of stress plateaus, samples started to deform heterogeneously, with stress decreasing to 679 MPa for Extruded-GM and 1008 MPa for ECAP-GM at a strain value of 20%. When the strain exceeded 20.0%, the stresses increased again because the sample surfaces contacted each other following fracture. Our analysis deliberately excluded this portion of the data.
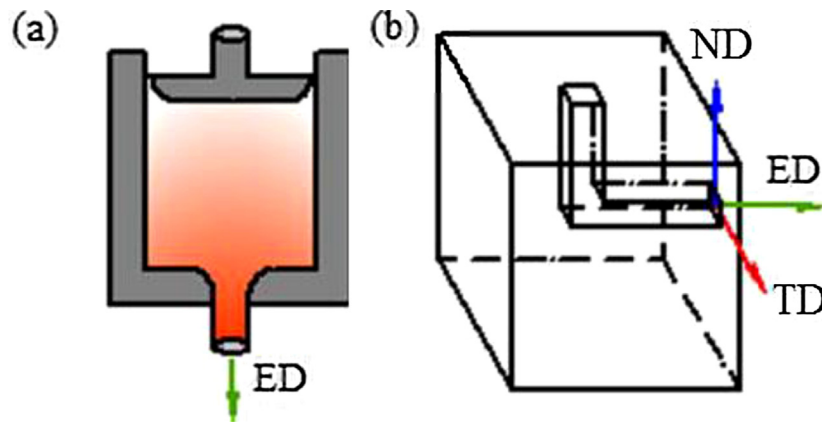
Fig. 1. Schematic diagrams of the material fabrication process and sample coordinate system. (a) The extrusion process with the green arrow indicating the extrusion direction (ED). (b) The equal channel angular pressing (ECAP) process with the sample coordinate system, in which the red, green and blue arrows represent the transverse direction (TD), extrusion direction (ED) and normal direction (ND), respectively.

Table 1
Mechanical parameters from engineering and true stress-strain curves of the impacted Extruded-GM and ECAP-GM specimens.

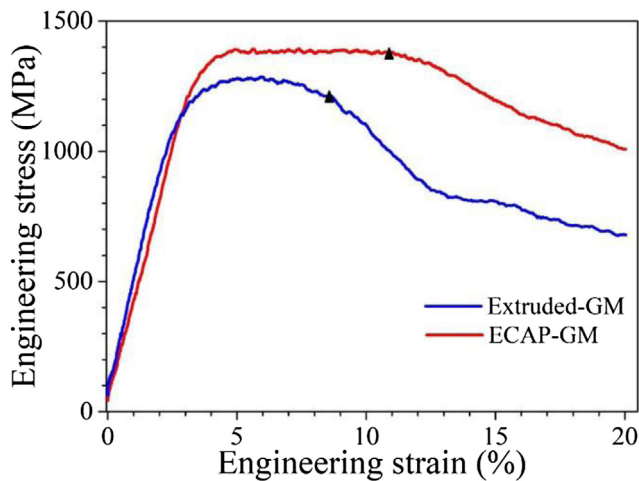|	End point of peak stress plateau				20% engineering strain			
	Engineeringstress (MPa)	Engineering strain (%)	True stress (MPa)	True strain (%)	Engineering stress (MPa)	Engineering strain (%)	True stress (MPa)	True strain (%)
Extruded-GM	1212	8.6	1108	8.2	679	20.0	543	18.3
ECAP-GM	1381	11.0	1228	10.5	1008	20.0	806	18.3

Fig. 2. Engineering strain-stress curves of Extruded-GM (blue line) and ECAP-GM (red line). The black triangles marked the ends of the stress plateaus.

Fig. 3. (a) The IPF-Z orientation map from the ED-TD plane of Extruded-GM, inset is the IPF-Z coloring code; (b) inverse pole figures of (a); (c) the zoom-in view and local misorientation map of Extruded-GM, blue, green and red colors in the rainbow bar represent low (< 1°), medium (from 1° to 3°) and high (from 3° to 5°) misorientations; (d) GBs displayed on (c); (e) the recrystallization map of (c), blue, yellow, red colors indicate recrystallized, substructured and deformed areas, respectively.

3.2. Microstructures of the as-processed Extruded-GM

All orientation maps presented in this paper are indicated by the inverse pole figure coloring scheme relative to the axis Z of chamber coordinate system (IPF-Z coloring code). The color code is inserted at the lower left corner of Fig. 3(a), in which red, green and blue indicate grains having <001>, <101> and <111> directions parallel to the axis Z. Additionally, black lines in the orientation map represent high angle GB (HAGB, misorientation θ > 10°) and silver lines represent low angle GB (LAGB, 2° < θ < 10°).

3.2.1. Grain size and texture

Fig. 3(a) shows the orientation map of an area from the ED-TD plane of the Extruded-GM material; the TD is horizontal in this map and the ED is vertical, as marked in the figure. Two categories of grains can be identified by their distinct difference in grain size. The
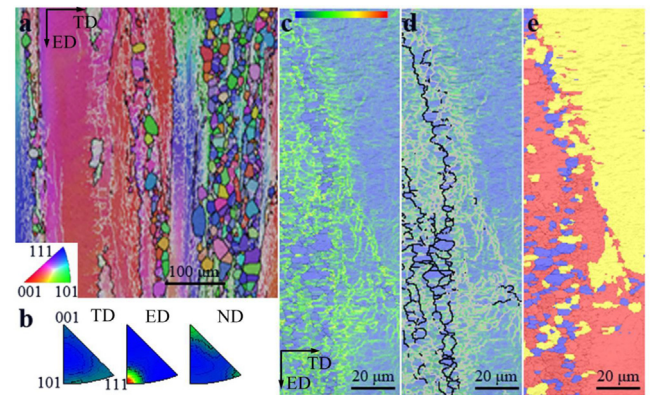
first category consisted of elongated grains which were formed during the extrusion process. Their lengths were beyond our scanning area, while their widths were about 200 μm. The second category included small grains created via recrystallization due to the combined effects of temperature and plastic deformation during extrusion. Newly recrystallized grains were equiaxed with grain sizes ranging from several micrometers to tens of micrometers.

Inverse pole figures of the Extruded-GM are shown in Fig. 3(b). The dominant texture was a fiber <110> texture along the ED. This result is consistent with the extrusion texture reported for bcc metals and alloys [45]. In addition, <100> and <111> textures were observed on the ND. Minor and scattered <110> and <111> textures extended on the TD.

3.2.2. Stored energy

Stored energy is related with dislocation accumulation which could alter local crystal orientation and be characterized by EBSD local misorientation. The local misorientation parameter can be obtained by misorientation of every EBSD scanning pixel compared with its surrounding pixels. Fig. 3(c) illustrates local misorientation in an area from the Extruded-GM. The color code bar on the top represents the level of misorientation. Red points on the map stand for large misorientation from 3° to 5° from surrounding points while green and blue points represent median (from 1° to 3°) and low (< 1°) misorientations. Fig. 3(d) displays LAGB (white lines) and HAGB (black lines) in Fig. 3(c). On the right side of Fig. 3(c) and (d), blue color dominates, indicating the average misorientation in this area is <1°; moreover, green network at the blue interior was found, which is subgrain boundary formed due to the rearrangement of dislocations. On the left part, green color with misorientation from 1° to 3° is dominant coexisting with some small blue patches with misorientation under 1° (Fig. 3(c)). From Fig. 3(d), these small blue patches are recrystallized grains with HAGBs. In addition, a LAGB network (white lines) is distributed within the green area in the left part, suggesting slight deformation. Due to temperature, blue recrystallized grains have low dislocation density and local misorientation inside. In related work, Hughes and Hansen have proposed the theory of GB and misorientation induced by geometrically necessary dislocations [47–50].

3.2.3. Recrystallization

Fig. 3(e) depicts deformed, substructured and recrystallized areas in Fig. 3(c), which were measured via the internal average misorientation angle within the grains. The internal average misorientation angle was obtained from the total local misorientation values divided by pixel number within a grain. Since the misorientation of sub-grain boundary (boundary between two neighboring sub-grains) is usually smaller than 2°, a grain is defined as "substructured"(yellow area) when internal average misorientation is less than 2°. When the average misorientation angle in a grain exceeds 2° due to severe dislocation accumulation, the grain is classified as "deformed"(red area). "Recrystallized"(blue area) grains have little or no intra-grain deformation and therefore little or no average internal misorientation. For a well-defined grain here, its mis-orientation should exceed 10°.

From Fig. 3(e), one can see that the left red area was deformed part with higher dislocation density and larger local misorientation of >2°. Moreover, due to the combined effect of plastic deformation and temperature, the blue recrystallized area was equiaxed shape with well-defined boundary and free of dislocation or misorientation in the interior. These blue recrystallized grains in Fig. 3(e) correspond well with the blue patches in Fig. 3(c) and (d). In addition, the right yellow substructured area was consisted of subgrains which were formed via slight deformation induced the rearrangement of dislocations during extrusion. As stated earlier, the network of subgrain boundaries was also observed and is shown as a green network on the right part in Fig. 3(c) and (d).

3.3. Microstructures of the as-processed ECAP-GM

Fig. 4(a) presents an area from the ED-TD plane of ECAP-GM. Except for the elongated grains formed during extrusion process, sheared zones were induced by the shearing deformation in ECAP. Pole figures of ECAP-GM are given in Fig. 4(b). In ECAP-GM, <100> texture had strong tendency to move along the ED. There were also parts of them extending on the TD and ND. In addition, <110> texture tended to move towards the ND. In other words, deformation had driven originally ED-directed <110> texture towards the ND and originally ND-directed <100> texture towards the TD and ED. In cubic materials, it was reported that the initial texture has a
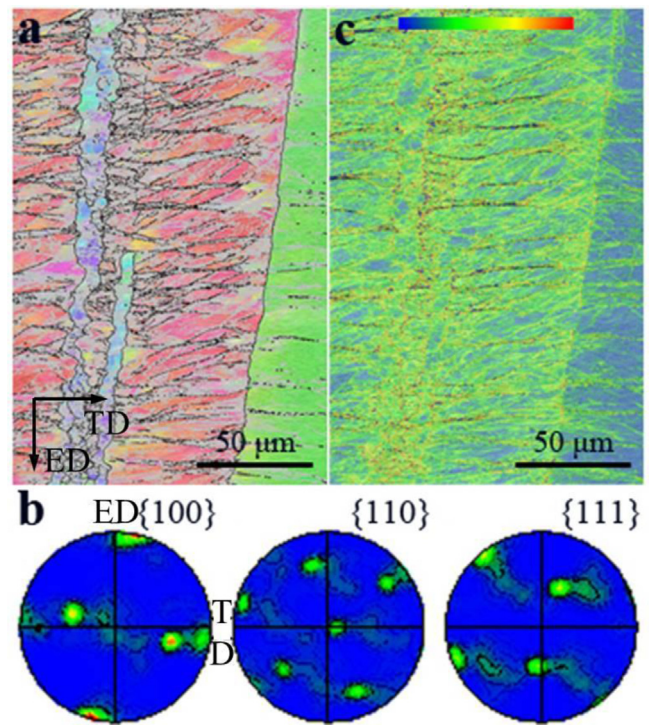

Fig. 4. (a) The IPF-Z orientation map of an area from the ED-TD plane of ECAP-GM; (b) pole figures of (a); (c) the local misorientation map of (a).

hereditary effect even following extensive deformation. For example, early work on torsion testing of fcc materials shows that initial texture effects can prevail up to a shear strain $\gamma = 2$ [46]. Moreover, textures generated from simple shearing, like torsion testing and ECAP, are generally not strong, and even a weak initial texture can possibly affect texture evolution during ECAP, up to the first and second pass [46]. This is consistent with our results which show that <110> texture is retarded in ECAP-GM. In addition, during ECAP processing, the die angle, ECAP route and pass number were reported to significantly impact texture evolution. Specifically, the die angle will affect the positions of texture components and the degree of texture evolution [46]. In ideal ECAP conditions, any rotation of the sample around the ND can hardly change the texture symmetry, while sample rotation around any other axis leads immediately to the loss of symmetry [46].

Fig. 4(c) illustrates the local misorientation of Fig. 4(a). Compared with Fig. 3(c), the dislocation density was higher because green color (median misorientation from 1° to 3°) dominates Fig. 4(c) and red color (high misorientation from 3° to 5°) was even observed along sheared zones. This could also be supported by a denser network of LAGB and HAGB in Fig. 4(a). The stored energy in ECAP-GM therefore is higher than that in Extruded-GM.

3.4. Microstructures of post-loading Extruded-GM-DY and ECAP-GM-DY

3.4.1. Grain size and texture

Fig. 5(a) and (b) is the orientation maps of the ND–TD planes of Extruded-GM-DY and ECAP-GM-DY. The TD is horizontal and the normal direction (ND) is vertical in these figures. According to the morphology, ASBs were formed in the matrix of both Extruded-GM-DY and ECAP-GM-DY. Moreover, between the ASBs and the matrix, there were small transition areas which consisted of elongated grains and subgrains with a width of 1−3 μm, as highlighted by "T". In addition, the matrix areas close to ASBs likely experienced some plastic deformation during dynamic loading. The grain size of
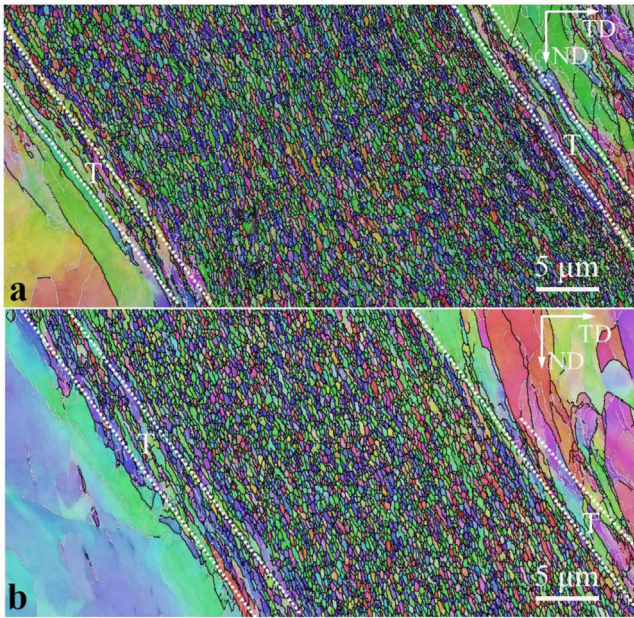
Fig. 5. (a, b) The IPF-Z orientation maps of areas crossed by ASBs from the ND-TD plane of Extruded-GM-DY and ECAP-GM-DY, respectively [1]. The transition areas were enveloped by dashed lines and highlighted by "T".

the matrix varied from several micrometers to a few tens micrometers. As most of the plastic deformation is concentrated in the small and localized band (ASBs), substantial grain refinement was found in ASBs, as indicated by Fig. 6(a) and (c). UFGs were formed inside the ASBs of Extruded-GM-DY and ECAP-GM-DY. The grain size distributions of the UFGs are given in Fig. 6(b) and (d). As the step size of EBSD analysis was 50 nm, data of grain size less than 250 nm was

not very reliable and was thus abandoned in our analysis. However, it is worth noting that the grain sizes inside the ASBs were certainly below 1 μm.

The pole figures of ASBs in Extruded-GM-DY and ECAP-GM-DY are shown in Fig. 7(a) and (c) and the pole figures of the matrix areas in Extruded-GM-DY and ECAP-GM-DY are given in Fig. 7(b) and (d), respectively. Since the characterized areas are the ED-TD planes and the ND-TD planes on the as-processed GM and post-loading GM, this changes the geometry relationships between the sample coordinates and the chamber coordinates. In Fig. 7(a) and (c), the pole figures were composed of several clusters indicating several preferred directions. Taking the cluster density into consideration, each component should contain a considerable quantity of grains with preferred orientations. The ASBs, therefore, were composed of various texture components which further consisted of a considerable number of grains. Undoubtedly, the process and mechanism of grain refinement in ASBs have strongly affected the texture evolution within the ASBs. However, it is worth noting that the clusters had the tendency to move along the shear direction (SD) and the direction normal to shear plane (NSP) in those pole figures. This implies that shearing also exerted a significant influence on these texture components. In Fig. 7(b) and (d), the <100> texture component in the matrix was greatly affected by shearing deformation. One texture component extended on the shear direction, while the other moved along the direction normal to the shear plane. In addition, a significant number of grains still maintained their <110> in the ED, as proved by the cluster at the center of the {110} pole figure.

3.4.2. Stored energy and recrystallization

Fig. 8(a) and (b) illustrate the local misorientations on the ASBs of Extruded-GM-DY and ECAP-GM-DY. Local misorientaion in the matrix was mostly in the low range except some network of median-level misorientations due to low dislocation density and
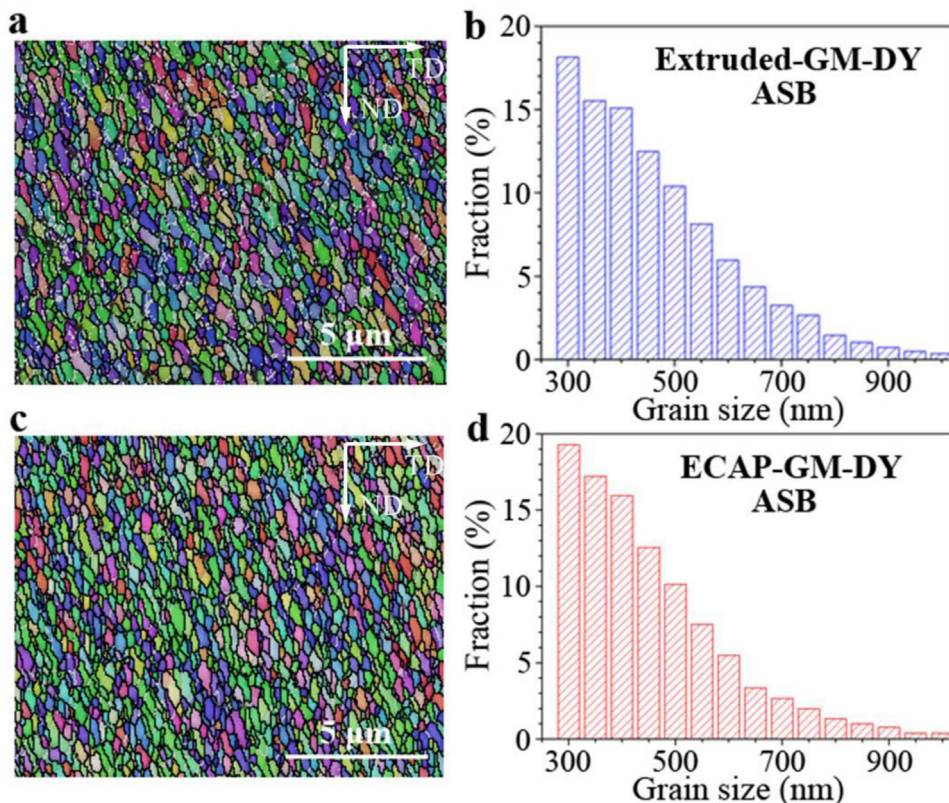

Fig. 6. (a, c) The zoom-in views of areas in the ASBs of Extruded-GM-DY and ECAP-GM-DY; (b, d) the grain size distributions in the ASBs of Extruded-GM-DY and ECAP-GM-DY.
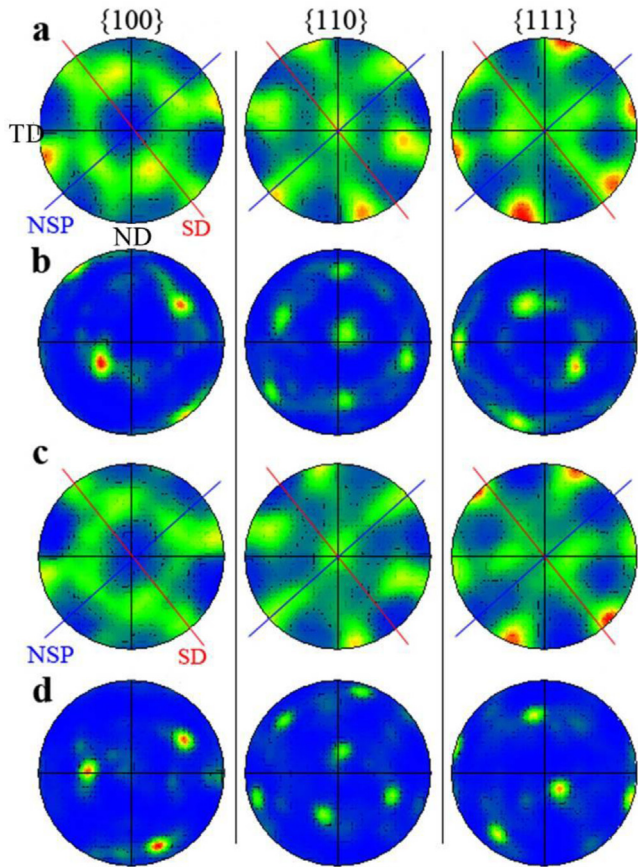
Fig. 7. (a, c) Pole figures of the ASBs in Extruded-GM-DY and ECAP-GM-DY, SD and NSP represent shear direction and the direction being normal to shear plane; (b, d) pole figures of matrix areas in Extruded-GM-DY and ECAP-GM-DY.

minor plastic deformation. The GB distribution maps in Fig. 8(c) and (e) also indicated the significant role of subgrain boundaries and LAGBs in the matrix. In the ASB of Extruded-GM-DY, green color dominates, indicating that there existed severe misorientations due to high dislocation density in each individual grain and a high density of LAGBs and subgrain boundaries. Fig. 8(d) further confirmed the above results and a large portion (> 60%) of LAGBs were formed in the GB distribution. However, for the ASB of ECAP-GM-DY, blue

color dominated which means a low dislocation density and low misorientations in each individual grain. Fig. 8(f) further verified the above result and showed high ratio (– 70%) of HAGBs in the GB distribution.

Fig. 9(a) and (b) are the recrystallization maps corresponding to the ASBs of Extruded-GM-DY and ECAP-GM-DY with the same color code as Fig. 3(e). The yellow matrix contained subgrains and the internal misorientation inside each subgrain is less than 2°, consistent with the above analysis. Red deformed grains dominated the ASB of Extruded-GM-DY as shown in Fig. 9(a) while blue recrystallized grains dominated the ASB of ECAP-GM-DY as presented in Fig. 9(b). The fraction of deformed UFGs in Extruded-GM-DY was 81.4% as illustrated in Fig. 9(c), while that in ECAP-GM-DY was just 8% as shown in Fig. 9(d). The significant internal misorientations in Extruded-GM-DY agreed well with the large fraction of LAGBs (– 10%) and subgrain boundaries (– 53%) in Fig. 8(d). The overwhelming statistical ratio of blue recrystallized grains in ECAP-GM-DY (72%), given in Fig. 9(d), also agreed well with the results in Fig. 5(b) and Fig. 8(b).

4. Discussion

Our above experimental results indicate that: (i) the ECAP-GM had a larger compressive uniform deformation than the Extruded-GM, (ii) ECAP process generated more defects (higher local misorientation and denser network of LAGBs and HAGBs) and higher level of stored energy relative to those in the initial Extruded-GM, (iii) although ASBs were generated in both of ECAP-GM-DY and Extruded-GM-DY, the ASB in former sample were mainly composed of recrystallized UFGs, while the ASB in the latter sample mostly consisted of deformed UFGs. In the following, we discuss the different formation mechanisms of the different UFG microstructures in the ASBs of the Extruded-GM and ECAP-GM specimens by calculating the temperature rises during impact deformation.

Inspection of the published literatures reveal that although the global adiabatic temperature rise of the entire specimen is only a few tens of degrees, the adiabatic temperature rise inside an ASB can be as high as > 1273 K, depending on loading conditions and materials parameters [51]. The high temperature causes recrystallization inside the ASBs, and this well-known ASB mechanism is thought to be responsible for the recrystallized UFGs in the ASB of the ECAP-GM observed in this research. However,
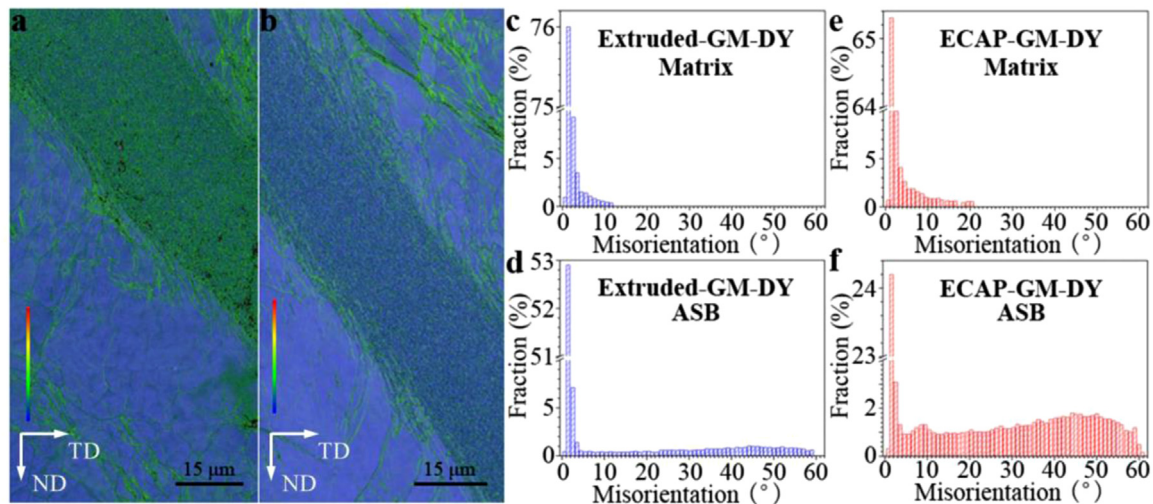

Fig. 8. (a, b) The local misorientation maps of the ASBs of Extruded-GM-DY and ECAP-GM-DY; (c, e) GB distributions of matrix areas in Extruded-GM-DY and ECAP-GM-DY; (d, f) GB distributions of ASBs in Extruded-GM-DY and ECAP-GM-DY.
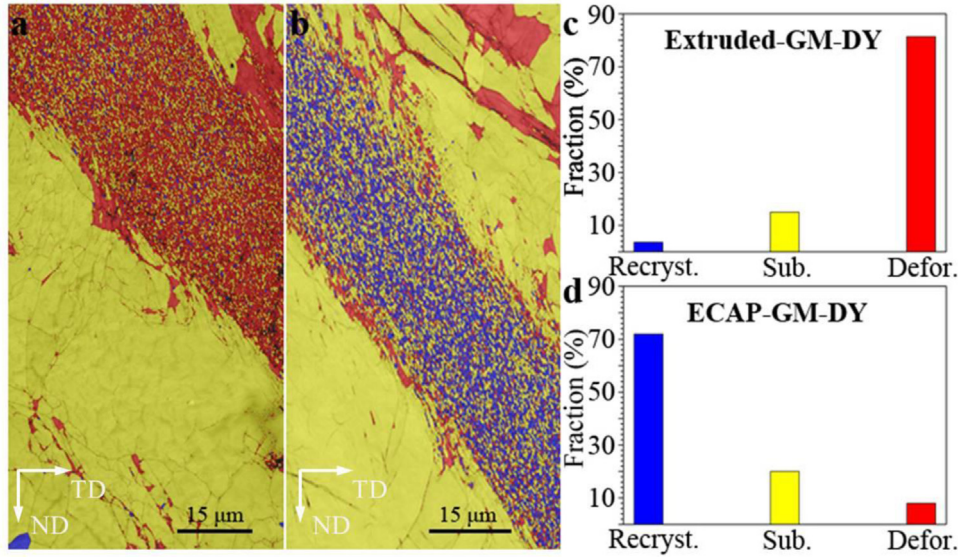
Fig. 9. (a, b) The recrystallization maps of the ASBs of Extruded-GM-DY and ECAP-GM-DY; (c, d) statistic fractions of recrystallized area (Recryst.), substructured area (Sub.) and deformed area (Defor.) in Fig. 9(a, b).

the deformed UFGs in the ASB of Extruded-GM-DY suggested a lower temperature rise in the ASB relative to a recrystallization temperature of $0.5T_{\rm m}$ ($T_{\rm m}$ is the melting temperature). In the following, we attempt to evaluate the temperatures from the beginning of plastic deformation to the failure points, paying particular attention to the maximum temperature reached during the ASB formation, in an effort to provide insight into the mechanisms that govern ASB formation in the Extruded-GM-DY and ECAP-GM-DY.

4.1. Temperature rise

The temperature in a deforming gauge section can be monitored in real-time, using an array of high-speed infrared detectors synchronized with an SHPB apparatus [25,52,53]. However, this technique can only accurately measure the surface temperature of the sample and might underestimate the adiabatic temperature rise inside of the ASBs. In fact, measuring the actual temperature rise inside an ASB has remained a formidable challenge. Alternatively, a number of semi-empirical formulas have been proposed to predict the temperature rise in the ASBs. The essential part of such semi-empirical formulas is the calculation of the work or energy involved in the process of plastic deformation. In a frequently used formula for the calculation of adiabatic temperature rise described in Ref. [54], the measured true stress and true strain are applied to calculate the average and global temperature rise of the entire sample before the initiation of ASBs, and the shear stress and shear strain are employed to calculate the temperature rise within an ASB. The shear stress can be derived from the experimental parameters and the shear strain can be determined from the flow lines of the ASBs [54]. However, it is difficult to measure the flow lines by EBSD characterization, as discussed in our earlier work [1]. Due to such limitation, it is necessary to develop a new method to establish a more accurate calculation of the temperature rise associated with ASBs.

In the literatures, inhomogeneous deformation begins at the end of the stress plateaus in the engineering stress-strain curves since flow softening is triggered from then on [25]. Therefore, energy,

from the end point of stress plateau to the point of failure, is empirically used to calculate the temperature rise in the ASBs as follows [55]:

$$\rho \cdot V_{\rm rise} \cdot c_{\upsilon} \cdot \Delta T = \eta \cdot V_{\rm work} \cdot \int_{\varepsilon_{\rm s}}^{\varepsilon_{\rm e}} \sigma {\rm d}\Gamma \qquad (1)$$

where $V_{\rm rise}$ is the volume of temperature rise, $V_{\rm work}$ the volume providing work, η the conversion fraction of heat converted from the mechanical work (0.9 in this work), σ, ε, ρ and c_{υ} are respectively the true stress, true strain, density and specific heat. Deformation stages can be easily recognized in the engineering stress-strain curves, and their corresponding true counterparts listed in Table 1. were used for our calculations. In our calculations for Ti-23Nb-0.7Ta-2Zr-O we assumed, $\rho = 5500\,{\rm kg/m^3}$ and $c_{\upsilon} = 528\,{\rm J/(kg\,^\circ C)}$.

Fig. 10 shows the temperature versus engineering strain and temperature versus time curves for the Extruded-GM-DY and ECAP-GM-DY. The data reveals the following points. First, when the GM was deformed uniformly, $V_{\rm rise}$ equaled to $V_{\rm work}$, and the overall or global temperature of the entire sample is estimated to be – 321 K and 331 K for Extruded-GM (8.6% strain) and ECAP-GM (11.0% strain) as indicated in Fig. 10(a). Second, when the ASBs started to form, plastic deformation was localized in the small band, and $V_{\rm work}$ /$V_{\rm rise}$, calculated from the ratio of ASB volume and sample volume in Extruded-GM-DY and ECAP-GM-DY, were 12.4 and 34.0 for Extruded-GM and ECAP-GM, respectively. Third, as the deformation zone became severely localized, the temperature soared after the onset points. Fourth, the slope of ECAP-GM-DY curve was larger than that of the Extruded-GM-DY counterpart, because the $V_{\rm rise}$ of ECAP-GM is much smaller than that of Extruded-GM. In other words, the ASB of ECAP-GM-DY has a smaller volume. Therefore, the temperature rise is more localized in ECAP-GM-DY. The temperatures were calculated to be 608 K and 1159 K in ASBs of Extruded-GM-DY and ECAP-GM-DY at the strain of 20%, respectively. It is worth noting that the actual value of temperature is affected by many factors such as material properties, microstructure, stress state and loading conditions [20,56]. Additionally, there is a temperature gradient across ASBs since the shear
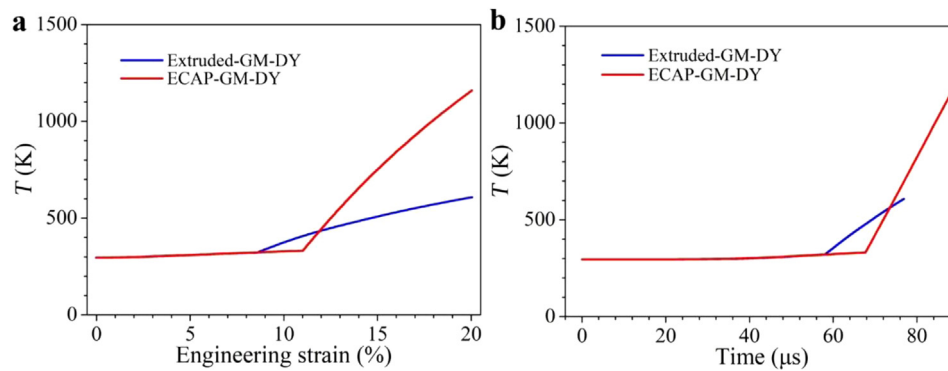
Fig. 10. (a) The temperature versus engineering strain of Extruded-GM-DY (blue line) and ECAP-GM-DY (red line) and (b) the temperature (T) vs time of Extruded-GM-DY (blue line) and ECAP-GM-DY (red line).

strain experienced in the center of ASBs was much higher than that corresponding to the ASB/matrix boundary.

4.2. Microstructural softening and thermal effect

On the basis of the above calculations, the overall temperatures of 321 K and 331 K for the Extruded-GM-DY and ECAP-GM-DY at the beginning of the ASBs were much lower than the thermal softening temperature ($0.5T_{m}$, the T_{m} of Ti-23Nb-0.7Ta-2Zr-O is about 2132 K) required for dynamic recrystallization [57–59], suggesting some sort of microstructural softening mechanism. Moreover, the interference of shock waves caused by the coincidence of shock waves on specific regions of the microstructure are likely to have unanticipated effects [20]. The plastic deformation localized in the specific coincidental areas of Extruded-GM-DY and ECAP-GM-DY also likely exerted large strains on these areas and contributed to the emergence of ASBs with substantial grain refinement. The calculated low temperature (608 K) within the ASB of the Extruded-GM is consistent with the observation of an insignificant ratio of recrystallized grains (3.6%), and vice versa for the ECAP-GM. In fact, even if all the plastic deformation was concentrated on the ASB of the Extruded-GM-DY from the yielding point on, the maximum temperature in the ASB would be only 898 K, still lower than the critical temperature required for recrystallization, which further supports the notion of a microstructure softening mechanisms leading to the formation of ASBs.

Interrupted dynamic tests were carried out by Rittel et al. [27], where they proposed that the "dynamic stored energy of cold work" is a good criterion to predict ASB formation. Their experimental results indicate that the final failure strain and the ASB onset strain of the tested metals are not affected by the dynamic interruption of the tests. Since the maximum temperatures achieved were obviously different for interrupted tests at different strains, thermal effect can hardly play an important role for the ASB formation. Their work demonstrates that the dynamic stored energy (or strain energy) is crucial for the initiation of ASBs. Similar results have been observed in cold-rolled tungsten [35] and a Cu alloy with tailored stacking fault energy [60]. Recent work by Langer and co-worker based on the notion of "effective temperature" suggests that adiabatic temperature rise is not the cause of the formation of ASBs in visco-plastic solids [61–63]. On the contrary, the microstructure softening is the root cause for the formation of ASBs followed by the adiabatic temperature rise. In this context, the work of Guo et al. provides experimental support for Langer's theory. Guo et al. reported that temperature rise reaches its maximum about 30 μs after ASB formation during the dynamic impact of pure titanium [25,53]. The time sequence of ASB formation and temperature rise indicates thermal softening should not be the primary reason for ASB initiation. All these experimental results are consistent with

our findings that the formation of ASBs occurs via a microstructural softening mechanism at relatively low temperatures.

In fact, Meyers et al. proposed a theory for recrystallization within ASBs [57]. Their theory is often referred to be the "rotational recrystallization mechanism", which takes dislocation energetics and GB reorientation as the reasons for grain refinement in ASBs [57]. According to this mechanism, a homogeneous distribution of dislocations rearranges itself into elongated dislocation cells. As the deformation and misorientation continue, these cells become elongated subgrains. The elongated subgrains further break up into equiaxed micrograins [57]. Recrystallization can be initiated by large strains and an appropriate temperature, and recrystallized UFGs were observed in the ASBs of Ti, Cu, Al-Li and Ta [57]. The grain rotation phenomenon has also been observed in our earlier work [1]. The rotational recrystallization mechanism explains our observation that high fraction (72%) of recrystallized UFGs formed in the ASB of ECAP-GM-DY, while high fraction of deformed UFGs were formed by rotational refinement mechanism in the ASB of Extruded-GM-DY. Because much more dislocations and strain energy were generated during the ECAP process, it provided a more favorable precondition for recrystallization during the later-on stage for the propagation and multiplication of ASBs. As a result, with the appropriate temperature in ASBs being higher than $0.5T_{c}$ (2132 K), rotational recrystallization mechanism takes effect. Therefore, the grain refinement of ECAP-GM-DY goes to further stage of dynamic recrystallization, while that for Extruded-GM-DY is still on the stage of deformed grains because the critical temperature was not attained. Again, the mechanism proposed by Meyers et al. [57], in combination with our observations, demonstrates that large deformation or strain energy plays a more critical role than thermal softening during ASB initiation.

4.3. Microstructural evolutions of ASBs

UFGs in the ASBs originated from the high strain and high strain rate deformation. As microstructural softening is responsible for the initiation of ASBs, plastic strain and/or thermal effect are the factors governing the subsequent propagation and multiplication of ASBs. According to the calculated temperature curves shown in Fig. 10, ECAP-GM-DY has undergone a higher temperature at the ASB onset point than Extruded-GM (331 versus 321 K). The higher temperature was caused by more stored energy induced by the ECAP in combination with the higher and longer stress plateau. Considering the entire sample volume, the temperature difference was only 10 K. After the onset of ASB formation, plastic deformation was localized within the ASBs. A large number of recrystallized UFGs were created in the ASB of the ECAP-GM because of the combined effect of localized plastic deformation and appropriate temperature (1159 K). While the insufficient temperature rise in

the ASB of Extruded-GM formed the deformed UFGs in the ASB. The higher stress plateau and uniform deformation strain of ECAP-GM relative to those of Extruded-GM were attributed to the ECAP process which refined the coarse grains and effectively homogenized the microstructure.

5. Conclusions

In this work, GM has been fabricated by conventional extrusion and ECAP. Split-Hopkinson Pressure Bar technique was used to evaluate the mechanical properties of the GM specimens. Based on mechanical properties, EBSD characterization and discussions, the following conclusions can be drawn:

(1) The ASB of Extruded-GM-DY was dominated by deformed UFGs (81.4%) which individually had significant dislocation density and internal misorientations, in contrast, the ASB of ECAP-GM-DY was composed of a high fraction (72%) of recrystallized UFGs which had a low dislocation density and small internal misorientation.
(2) The maximum temperature was higher in the ASB of ECAP-GM-DY (1159 K) than that in the ASB of Extruded-GM-DY (608 K), resulting in different UFGs in the ASBs. The ECAP-GM-DY material reached the critical temperature of recrystallization while the temperature of the Extruded-GM-DY did not.
(3) On the basis of the analysis of microstructures and the corresponding mechanical behavior, the initiation of ASBs is attributed to a mechanism involving microstructural softening.

Acknowledgements

References

[1] S.L. Liu, Z.L. Pan, Y.H. Zhao, T. Topping, R.Z. Valiev, X.Z. Liao, E.J. Lavernia, Y.T. Zhu, Q. Wei, Acta Mater. 132 (2017) 193–208.
[2] T. Saito, Science 300 (2003) 464–467.
[3] J.P. Liu, Y.D. Wang, Y.L. Hao, Y. Wang, Z.H. Nie, D. Wang, Y. Ren, Z.P. Lu, J. Wang, H. Wang, X. Hui, N. Lu, M.J. Kim, R. Yang, Sci. Rep. 3 (2013) 1–7.
[4] T. Furuta, S. Kuramoto, J.W. Morris, N. Nagasako, E. Withey, D.C. Chrzan, Scr. Mater. 68 (2013) 767–772.
[5] K.Y. Xie, Y. Wang, Y. Zhao, L. Chang, G. Wang, Z. Chen, Y. Cao, X. Liao, E.J. Lavernia, R.Z. Valiev, B. Sarrafpour, H. Zoellner, S.P. Ringer, Mater. Sci. Eng. C 33 (2013) 3530–3536.
[6] Y.L. Hao, S.J. Li, S.Y. Sun, C.Y. Zheng, R. Yang, Acta Biomater. 3 (2007) 277–286.
[7] T. Li, J.W. Morris, N. Nagasako, S. Kuramoto, D.C. Chrzan,Phys. Rev. Lett. 98 (2007), 105503.
[8] M.Y. Gutkin, T. Ishizaki, S. Kuramoto, I.A. Ovid'ko, N.V. Skiba, Int. J. Plast. 24 (2008) 1333–1359.
[9] S. Kuramoto, T. Furuta, J. Hwang, K. Nishino, T. Saito, Mater. Sci. Eng. A 442 (2006) 454–457.
[10] Y.L. Hao, S.J. Li, B.B. Sun, M.L. Sui, R. Yang,Phys. Rev. Lett. 98 (2007), 216405.
[11] M.Y. Gutkin, T. Ishizaki, S. Kuramoto, I.A. Ovid'ko, Acta Mater. 54 (2006) 2489–2499.
[12] H. Xing, J. Sun, Q. Yao, W.Y. Guo, R. Chen,Appl. Phys. Lett. 92 (2008), 151905.
[13] H. Tobe, H.Y. Kim, T. Inamura, H. Hosoda, S. Miyazaki, Acta Mater. 64 (2014) 345–355.
[14] H. Xing, J. Sun, Appl. Phys. Lett. 93 (2008) 31908.
[15] Y. Yang, S.Q. Wu, G.P. Li, Y.L. Li, Y.F. Lu, K. Yang, P. Ge, Acta Mater. 58 (2010) 2778–2787.
[16] P. Castany, M. Besse, T. Gloriant,Phys. Rev. B 84 (2011), 020201.
[17] Y.B. Wang, Y.H. Zhao, Q. Lian, X.Z. Liao, R.Z. Valiev, S.P. Ringer, Y.T. Zhu, E.J. Lavernia, Scr. Mater. 63 (2010) 613–616.
[18] J.P. Cui, Y.L. Hao, S.J. Li, M.L. Sui, D.X. Li, R. Yang,Phys. Rev. Lett. 102 (2009), 045503.
[19] S.J. Li, R. Yang, M. Niinomi, Y.L. Hao, Y.Y. Cui, Z.X. Guo, Mater. Sci. Technol. 21 (2005) 678–686.
[20] B. Dodd, Y. Bai, Adiabatic Shear Localization: Frontiers and Advances, 2nd ed., Elsevier, Amsterdam, 2012, pp. 111–164.
[21] B. Dodd, Adiabatic Shear Localization Occurrence, Theories and Applications, Elsevier, Oxford, 2012, pp. 24–44.
[22] S.M. Walley, Metall. Mater. Trans. A 38 (2007) 2629–2654.
[23] R.W. Armstrong, S.M. Walley, Int. Mater. Rev. 53 (2008) 105–128.
[24] C. Zener, J.H. Hollomon, J. Appl. Phys. 15 (1944) 22–32.
[25] Y. Guo, Q. Ruan, S. Zhu, Q. Wei, H. Chen, J. Lu, B. Hu, X. Wu, Y. Li, D. Fang,Phys. Rev. Lett. 122 (2019), 015503.
[26] D. Rittel, L.H. Zhang, S. Osovski,Phys. Rev. Appl. 7 (2017), 044012.
[27] D. Rittel, Z.G. Wang, M. Merzer,Phys. Rev. Lett. 96 (2006), 075502.
[28] D. Rittel, P. Landau, A. Venkert,Phys. Rev. Lett. 101 (2008), 165501.
[29] S. Medyanik, W. Liu, S. Li, J. Mech. Phys. Solids 55 (2007) 1439–1461.
[30] S. Cheng, Y. Zhao, Y. Guo, Y. Li, Q. Wei, X.L. Wang, Y. Ren, P.K. Liaw, H. Choo, E.J. Lavernia, Adv. Mater. 21 (2009) 5001–5004.
[31] Q. Wei, D. Jia, K.T. Ramesh, E. Ma, Appl. Phys. Lett. 81 (2002) 1240–1242.
[32] Q. Wei, H. Zhang, B. Schuster, K. Ramesh, R. Valiev, L. Kecskes, R. Dowding, L. Magness, K. Cho, Acta Mater. 54 (2006) 4079–4089.
[33] Q. Wei, Z.L. Pan, X.L. Wu, B.E. Schuster, L.J. Kecskes, R.Z. Valiev, Acta Mater. 59 (2011) 2423–2436.
[34] Q. Wei, S. Cheng, K. Ramesh, E. Ma, Mater. Sci. Eng. A 381 (2004) 71–79.
[35] Q. Wei, L.J. Kecskes, K.T. Ramesh, Mater. Sci. Eng. A 578 (2013) 394–401.
[36] O. Engler, V. Randle, Introduction to Texture Analysis: Macrotexture, Microtexture, and Orientation Mapping, 2nd ed., CRC Press, Boca Raton, 2010, pp. 15–50.
[37] J.L. Sun, P.W. Trimby, F.K. Yan, X.Z. Liao, N.R. Tao, J.T. Wang, Acta Mater. 79 (2014) 47–58.
[38] Y. Xu, J. Zhang, Y. Bai, M.A. Meyers, Metall. Mater. Trans. A 39 (2008) 811–843.
[39] Q. Xue, J.F. Bingert, B.L. Henrie, G.T. Gray, Mater. Sci. Eng. A 473 (2008) 279–289.
[40] Q. Xue, G.T. Gray, B.L. Henrie, S.A. Maloy, S.R. Chen, Metall. Mater. Trans. A 36 (2005) 1471–1486.
[41] R.Z. Valiev, T.G. Langdon, Prog. Mater. Sci. 51 (2006) 881–981.
[42] Y.H. Zhao, X.Z. Liao, Z. Jin, R.Z. Valiev, Y.T. Zhu, Acta Mater. 52 (2004) 4589–4599.
[43] Q. Wei, T. Jiao, K. Ramesh, E. Ma, L. Kecskes, L. Magness, R. Dowding, V. Kazykhanov, R. Valiev, Acta Mater. 54 (2005) 77–87.
[44] Q. Wei, L. Kecskes, T. Jiao, K.T. Hartwig, K.T. Ramesh, E. Ma, Acta Mater. 52 (2004) 1859–1869.
[45] W.Y. Guo, H. Xing, J. Sun, X.L. Li, J.S. Wu, R. Chen, Metall. Mater. Trans. A 39 (2008) 672–678.
[46] I.J. Beyerlein, L.S. Toth, Prog. Mater. Sci. 54 (2009) 427–510.
[47] D.A. Hughes, N. Hansen, Acta Mater. 48 (2000) 2985–3004.
[48] D.A. Hughes, Q. Liu, D.C. Chrzan, N. Hansen, Acta Mater. 45 (1997) 105–112.
[49] D.A. Hughes, W.D. Nix, Mater. Sci. Eng. A 122 (1989) 153–172.
[50] B. Bay, N. Hansen, D.A. Hughes, D. Kuhlmann-Wilsdorf, Acta Metall. Mater. 40 (1992) 205–219.
[51] M.A. Meyers, Y.B. Xu, Q. Xue, M.T. Pérez-Prado, T.R. McNelley, Acta Mater. 51 (2003) 1307–1325.
[52] D. Rittel, Z.G. Wang, Mech. Mater. 40 (2008) 629–635.
[53] Y.Z. Guo, Q.C. Ruan, S.X. Zhu, Q. Wei, J.N. Lu, B. Hu, X.H. Wu, Y.L. Li,J. Mech. Phys. Solids 135 (2020), 103811.
[54] Y. Zheng, W. Zeng, Y. Wang, D. Zhou, X. Gao, J. Alloys. Compd. 708 (2017) 84–92.
[55] Y. Guo, Y. Li, Acta Mech. Solida Sin. 25 (2012) 299–311.
[56] D. Rittel, L.H. Zhang, S. Osovski, J. Mech. Phys. Solids 107 (2017) 96–114.
[57] M.A. Meyers, V.F. Nesterenko, J.C. LaSalvia, Q. Xue, Mater. Sci. Eng. A 317 (2001) 204–225.
[58] M.A. Meyers, V.F. Nesterenko, J.C. LaSalvia, Y.B. Xu, Q. Xue, J. Phys. IV France 10 (2000), Pr9-51–Pr9-56.
[59] J.A. Hines, K.S. Vecchio, Acta Mater. 45 (1997) 635–649.
[60] J. Li, Y. Li, C. Huang, T. Suo, Q. Wei, Acta Mater. 141 (2017) 163–182.
[61] J.S. Langer,Phys. Rev. E 95 (2017), 013004.
[62] J.S. Langer,Phys. Rev. E 94 (2016), 063004.
[63] J.S. Langer, E. Bouchbinder, T. Lookman, Acta Mater. 58 (2010) 3718–3732.